JWST Imaging of the Closest Globular Clusters – III.
Multiple Populations along the low-mass Main Sequence stars of NGC 6397

M. Scalco[1,2,⋆], M. Libralato[2], R. Gerasimov[3], L. R. Bedin[2], E. Vesperini[4], D. Nardiello[5,2], A. Bellini[6], M. Griggio[1,2,6], D. Apai[7,8], M. Salaris[9], A. Burgasser[10], and J. Anderson[6]

[1] Dipartimento di Fisica e Scienze della Terra, Università di Ferrara, Via Giuseppe Saragat 1, Ferrara I-44122, Italy
[2] Istituto Nazionale di Astrofisica, Osservatorio Astronomico di Padova, Vicolo dell'Osservatorio 5, Padova I-35122, Italy
[3] Department of Physics and Astronomy, University of Notre Dame, Nieuwland Science Hall, Notre Dame, IN 46556, USA
[4] Department of Astronomy, Indiana University, Swain West, 727 E. 3rd Street, Bloomington, IN 47405, USA
[5] Dipartimento di Fisica e Astronomia "Galileo Galilei", Università di Padova, Vicolo dellOsservatorio 3, I-35122, Padova, Italy
[6] Space Telescope Science Institute, 3700 San Martin Drive, Baltimore, MD 21218, USA
[7] Department of Astronomy and Steward Observatory, The University of Arizona, 933 N. Cherry Avenue, Tucson, AZ 85721, USA
[8] Lunar and Planetary Laboratory, The University of Arizona, 1629 E. University Blvd., Tucson, AZ 85721, USA
[9] Astrophysics Research Institute, Liverpool John Moores University, 146 Brownlow Hill, Liverpool L3 5RF, UK
[10] Department of Astronomy & Astrophysics, University of California, San Diego, La Jolla, California 92093, USA

ABSTRACT

Thanks to its exceptional near-infrared photometry, *JWST* can effectively contribute to the discovery, characterization, and understanding of multiple stellar populations in globular clusters, especially at low masses where the *Hubble Space Telescope* (*HST*) faces limitations. This paper continues the efforts of the *JWST* GO-1979 program in exploring the faintest members of the globular cluster NGC 6397. Here we show that the combination of *HST* and *JWST* data allows us to identify two groups of MS stars (MSa, the first-generation, and MSb, the second-generation group). We measured the ratio between the two groups and combined it with measurements from the literature focused on more central fields and more massive stars compared to our study. We find that the MSa and MSb stars are present in a ≈30-70 ratio regardless of the distance from the centre of the cluster and the mass of the stars used so far.

Key words. techniques: photometric; catalogues; Hertzsprung-Russell and colour-magnitude diagrams; Population II; star clusters: individual: NGC 6397

1. Introduction

Many important questions in the study of globular clusters (GCs) benefit from the exquisite near-infrared (NIR) astrometry and photometry *JWST* can provide. An example is the phenomenon of the multiple stellar populations (mPOPs; for a recent review, see Gratton et al. 2019).

Multiple stellar populations in GCs have been extensively studied for decades using the *Hubble Space Telescope* (*HST*, since Bedin et al. 2004). The ultraviolet (UV) and optical photometry provided by *HST* are particularly effective in disentangling the mPOPs in colour-magnitude (CMD) and colour-colour diagrams (e.g. Milone et al. 2017), spanning from the red-giant branch (RGB) to the main sequence (MS). However, as stars become fainter and redder, the effectiveness of UV filters diminishes. While optical filters maintain high photometric precision for observing MS stars, they alone may not always consent the identification of mPOPs as they lack the necessary information to differentiate stars with varying levels of oxygen, carbon, and nitrogen enhancement.

For these reasons, the analysis of mPOPs along the low-mass portion of the MS has predominantly relied on Near-Infrared (NIR) filters (see Scalco et al. 2024, and reference therein)

despite the inferior quality of *HST*'s NIR data compared to UV/optical detectors. The new generation of detectors onboard *JWST* now provides high-resolution, deep NIR images, enabling continued exploration of mPOPs along the MS of GCs and potentially advancing it further, as indicated by preliminary studies (Nardiello et al. 2022; Milone et al. 2023; Ziliotto et al. 2023; Cadelano et al. 2023).

This paper is the third of a series aimed at investigating one of the closest GCs to the Sun: NGC 6397. NGC 6397 is a close-by (2.48 kpc; Baumgardt & Vasiliev 2021), metal-poor ([Fe/H] = −2.02; Harris 1996, 2010) and old (age=12.6 Gyr; Correnti et al. 2018) GC. The first paper of the series, Bedin et al. (*accepted*; hereafter Paper I) used data from the Near Infrared Camera (NIRCam, Rieke et al. 2023) onboard *JWST* to characterize the white dwarf (WD) cooling sequence (CS) of this cluster, while the second paper, Gerasimov et al. (*submitted*; hereafter Paper II) is focused on the brown dwarfs (BDs) characterization of NGC 6397.

The presence of mPOPs in this stellar system was initially explored by Milone et al. (2012a) using data obtained with *HST*. Milone et al. (2012a) found that the MS of the cluster splits into two distinct components. One component (namely MSa) consists of a primordial population, resembling the composition of field stars. The other component (namely MSb) corresponds to

⋆ e-mail: michele.scalco@inaf.it

a second generation of stars characterized by enhanced sodium and nitrogen levels, reduced carbon and oxygen content, and a slightly increased helium abundance. The authors also found that MSb stars are more numerous (~70% of the total) than MSa (~30%). Here we make use of the astro-photometric catalogue of Paper I to analyze the mPOPs in the lower MS of NGC 6397.

The paper is organized as follows. Section 2 summarizes the data set and reduction; Section 3 describes the identification of the mPOPs, the isochrone fit and the radial and mass distribution of the two populations. Conclusions are presented in Section 4.

2. Observations and data reduction

The data were obtained as part of three programs:

- *HST* GO-10424 (PI: Richer; taken in ~2005.2). This set comprises images (with a combination of long and short exposure times) taken with Wide Field Channel (WFC) of the Advanced Camera for Surveys (ACS) in F606W and F814W filters;
- *HST* GO-11633 (PI: Rich; taken in ~2010.2). As before, this data set includes both long and short exposures in ACS/WFC F606W and F814W filters.
- *JWST* GO-1979 (PI: Bedin; taken in ~2023.2). The *JWST* data were obtained with the NIRCam camera in F150W2 and F322W2 filters.

Figure 1 shows the position of our datasets in the field-of-view (FOV) overlaid on a Digital Sky Survey[1] (DSS) image of NGC 6397.

We made use of calibrated but unresampled exposures (`_flc` and `_cal` fits files for *HST* and *JWST*, respectively). The data reduction was performed as described in Paper I, i.e., a combination of first- and second-pass photometry for *HST* (see Bellini et al. 2017a, 2018; Nardiello et al. 2018; Libralato et al. 2018, 2022; Scalco et al. 2021, for details) and *JWST* images (see Nardiello et al. 2022, 2023; Griggio et al. 2023; Libralato et al. 2023, 2024, for details). The astrometry was anchored to an absolute reference-frame system provided by the *Gaia* Data Release 3 (DR3) catalogue (Gaia Collaboration et al. 2016, 2023), and the photometry was calibrated to the VEGA-magnitude photometric system. Proper motions (PMs) were calculated by measuring the displacements between the *JWST* observations and the earliest *HST* observations, covering a temporal baseline of ~18 years. Detailed descriptions of the data sets and reduction are provided in Paper I.

The complete catalogue contains spurious detections such as cosmic rays or noise peaks in individual images. For this work, only a subset of well-measured cluster members was selected using the procedure outlined in Appendix A of Paper I. This section process is based on diagnostic parameters such as the quality-of-PSF fit parameter (`QFIT`), the excess/deficiency of the source's flux (`RADXS`, see Bedin et al. 2008), the local sky noise (`rmsSKY`), and the utilization of PM-based memberships criteria.

3. The split of the main sequence in NGC 6397 at lower stellar masses

Milone et al. (2012a) focused on the upper part of the MS within the mass range of ~0.56 to ~0.62 M$_\odot$, covering the central region of the cluster spanning from the centre to ~2 arcmin (equivalent to ~0.7r_h). In this study, we used our *HST* and *JWST* datasets
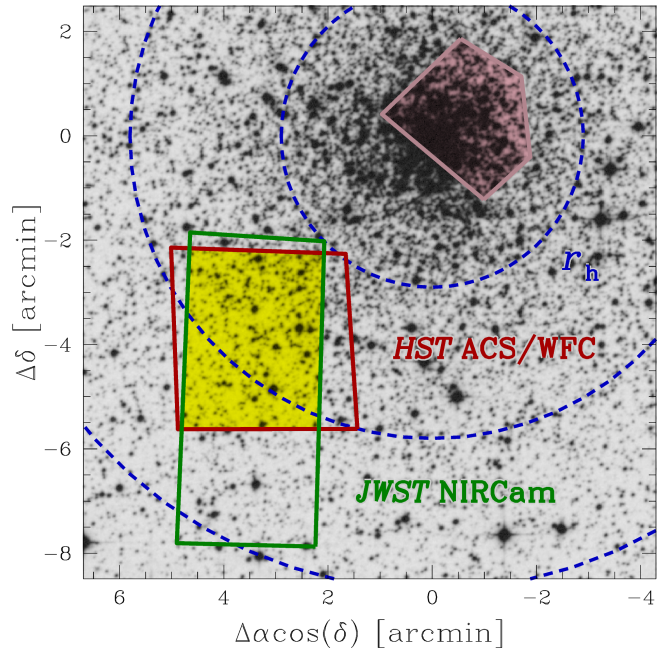
Fig. 1. Outlines of the ACS/WFC *HST* field observed under the GO-10424 and GO-11633 programs (in red) and the NIRCam *JWST* field observed under the GO-1979 program (in green), superimposed on a DSS image of NGC 6397. The region where the two data sets overlap is highlighted in yellow. We also show, in magenta, the field analysed in Milone et al. (2012a). Units are in arcmin measured from the centre of the cluster. The blue dashed circles mark the half-light radius (r_h = 2′.90; Harris 1996, 2010), 2 r_h and 3 r_h.

to investigate the two populations in the lower part of the MS, with masses ranging from ~0.09 to ~0.18 M$_\odot$, in an outer region spanning from ~3.2 to ~7 arcmin (equivalent to ~1.1r_h to ~2.4r_h) of NGC 6397.

We followed the methodology outlined by Milone et al. (2012b) (see also Sarajedini et al. 2007; Bellini et al. 2017b) to correct our photometry for differential reddening and photometric zero-point variations across the FOV. Then, we made use of two-pseudo-colour diagrams (TpCDs, see Milone et al. 2015a,b) to identify the two groups of stars in the MS of NGC 6397.

Panels (a) and (c) of Fig. 2 present the differential-reddening-and-zero-point-corrected m_{F150W2} versus $m_{F814W} - m_{F322W2}$ and m_{F150W2} versus $m_{F606W} - m_{F150W2}$ CMDs, respectively. In each CMD, we drew by hand two fiducial curves enclosing the MS (represented in green in panels (a) and (c)), that were used to rectify the sequence. The rectified CMDs are presented in panels (b) and (d), where $\Delta_{F814W-F322W2}$ and $\Delta_{F606W-F150W2}$ denote the $m_{F814W} - m_{F322W2}$ and $m_{F606W} - m_{F150W2}$ rectified and normalised pseudo-colours, respectively. Two sequences are faintly discernible in these diagrams, with one more populated on the red side of the plot and another less populated on the blue side of the plot.

We combined the two verticalized diagrams to construct the TpCD (panel e). Panel (f) displays the Hess diagram of the TpCD, colour-coded according to the local density of points. The colour goes from blue (lowest density) to green (average density) and red (highest density). Two components are visible: a clump around (0.65,0.60) representing the bump of MSb stars, and a tail extending towards the lower left part of the plot representing the MSa stars.

The black envelopes (hand-defined) in panel (g) tentatively delineate the two components in the TpCD, with MSa stars in blue and MSb stars in red. Stars outside the envelopes are rejected and represented in grey. We note that this represents an initial exploration, and a more detailed quantitative analysis will follow. The MSa component comprises 84 stars, representing the ~29%±4% of the total, while the MSb component comprises 201 stars, representing the ~71%±6% of the total. The errors in this and subsequent fractions are estimated by linear propagation of Poisson noise. These values are consistent with those reported in Milone et al. (2012a, ~30%±3% for the MSa and ~70%±3% for the MSb).

To better estimate the number of stars in each group while considering potential contamination between the populations, we adopted an alternative approach. Panel (a) of Fig. 3 displays the same TpCD as presented in panels (e) of Fig. 2. Initially, we fitted a straight line to the barycenters of the two populations in the TpCD (red dashed line), defining an angle θ with respect to the y-axis of the plot. Panel (b) shows the Δ_2 versus Δ_1 diagram obtained by a counterclockwise rotation of the TpCD by an angle θ around the point (0.5,0.5) so as to have the red line parallel to the y-axis. Finally, panel (c) presents the histogram of the Δ_2 distribution, with error bars representing Poisson errors. We fitted a double-Gaussian function to the histogram (depicted in grey), with the two components associated with MSa and MSb represented in blue and red, respectively. Once again, we determined that MSa and MSb comprise 29%±4% and 71%±6% of the total, respectively. These values are in agreement with those obtained previously.

3.1. Isochrone fit

At the range of effective temperatures considered in this study (lower MS below the MS knee, $T_{\mathrm{eff}} = 3000-4000$ K), broadband photometry is primarily influenced by the abundances of oxygen and titanium due to their role in molecular opacity (Gerasimov et al. 2024). Since the member-to-member scatter in [O/Fe] is the primary tracer of mPOPs in GCs, the individual populations can be identified in the CMD through a careful selection of photometric bands. The F322W2 band of NIRCam is particularly sensitive to the oxygen abundance due to its proximity to the fundamental vibrational bands of water near 3 μm (Jørgensen et al. 2001). The second band is most well-placed in the optical regime where H_2O absorption is minimal; however, wavelengths redder than ~ 0.7 μm are preferred to avoid the strongest electronic bands of TiO (Plez 1998). Of the filters considered in this work, the F814W band of ACS is therefore the most suitable. The oxygen content of individual stars in NGC 6397 can be inferred from the $m_{\mathrm{F814W}} - m_{\mathrm{F322W2}}$ colour with minimal systematic errors due to potentially unknown abundances of other elements.

To derive [O/Fe] from photometry, we first chose a model isochrone from the SANDee grid (Paper II; Alvarado et al. 2024, *in preparation*) that provides the best representation of the m_{F150W2} versus $m_{\mathrm{F814W}} - m_{\mathrm{F322W2}}$ and m_{F150W2} versus $m_{\mathrm{F606W}} - m_{\mathrm{F150W2}}$ CMDs. The chosen isochrone had [Fe/H] = -1.75 and [α/Fe] = 0.3. We then calculated 5 new model isochrones, varying [O/Fe] from -0.1 to 0.7 in steps of 0.2. The oxygen abundance was updated in the model atmospheres of the best-fit SANDee isochrone with $\log(g) \geq 4$, as well as the corresponding evolutionary models and boundary condition tables, following Gerasimov et al. (2024, 2022). For all new isochrones, we adopted the age of 12.6 Gyr from Correnti et al. (2018), the distance of 2.458 kpc from Baumgardt & Vasiliev (2021) and the optical reddening of $E(B - V) = 0.18$ from Gratton et al. (2003).

Table 1. Effect of choosing a different base model isochrone on the oxygen abundances of individual stars.

Change in base isochrone	Expected offset in [O/Fe]
Increase [α/Fe] by 0.2	+0.18
Decrease [Fe/H] by 0.2	−0.12
Increase $E(B - V)$ by 0.02	+0.09
Decrease age by 2 Gyr	−0.002

The isochrones are overplotted on the observed CMD in the upper panel of Figure 4.

Model isochrones for other oxygen abundances were obtained by linearly interpolating or extrapolating the mass-color and mass-magnitude relationships. The values of [O/Fe] for individual stars were then determined by searching for the interpolated isochrones that pass through the observed colours and magnitudes using Brent's method (Brent 1973). Overall, the oxygen abundance of ~ 300 members of NGC 6397 was measured. The distribution of these measurements is shown in the lower panel of Figure 4. The modal values of [O/Fe] for the two populations in the cluster were taken as the central values of the Gaussian components in a two-component Gaussian mixture fit to the inferred distribution. The fit was carried out using the expectation-maximization algorithm implemented in the scikit-learn package (Pedregosa et al. 2011). The two-component fit is shown in the lower panel of Figure 4. The modal values of [O/Fe] were estimated as 0.32±0.02 and 0.61±0.02 for the two populations. We also estimated the expected systematic offsets in our [O/Fe] measurements by comparing other possible choices for the best-fit SANDee isochrone to the isochrones used in this work. The results of this analysis are summarized in Table 1.

In Milone et al. (2012a), the representative [O/Fe] of the two populations were estimated as 0.1 and 0.45 based on the differences between observed colours and model atmospheres. The values found in this work are ~ 0.2 higher. This discrepancy can be reconciled only by reducing the metallicity of the best-fit isochrone by ~ 0.3 − 0.4, i.e., by setting it to [Fe/H] ~ −2. The implied lower metallicity would in fact be more consistent with other photometric (Correnti et al. 2018) and spectroscopic (Husser et al. 2016) estimates in the literature. The higher metallicity of NGC 6397 computed in this work near the end of the MS is likely due to imperfectly modelled physical processes in low-temperature stellar atmospheres such as depletion of gas-phase elements onto dust grains or non-equilibrium chemistry. A similar effect has been observed in a different NIRCam field of the cluster (Paper II).

The relative difference in [O/Fe] between the two populations is approximately equal to that determined by Milone et al. (2012a), confirming the correspondence between the cluster populations identified in both studies.

3.2. Radial and mass distribution of the two populations

Although the fractions of the two populations obtained in our study generally align with those reported by Milone et al. (2012a), we subdivided our sample to investigate potential dependencies of these populations on the radial distance from the cluster's centre and stellar mass. To do this, we considered the two groups of stars defined in panel (g) of Fig. 2.
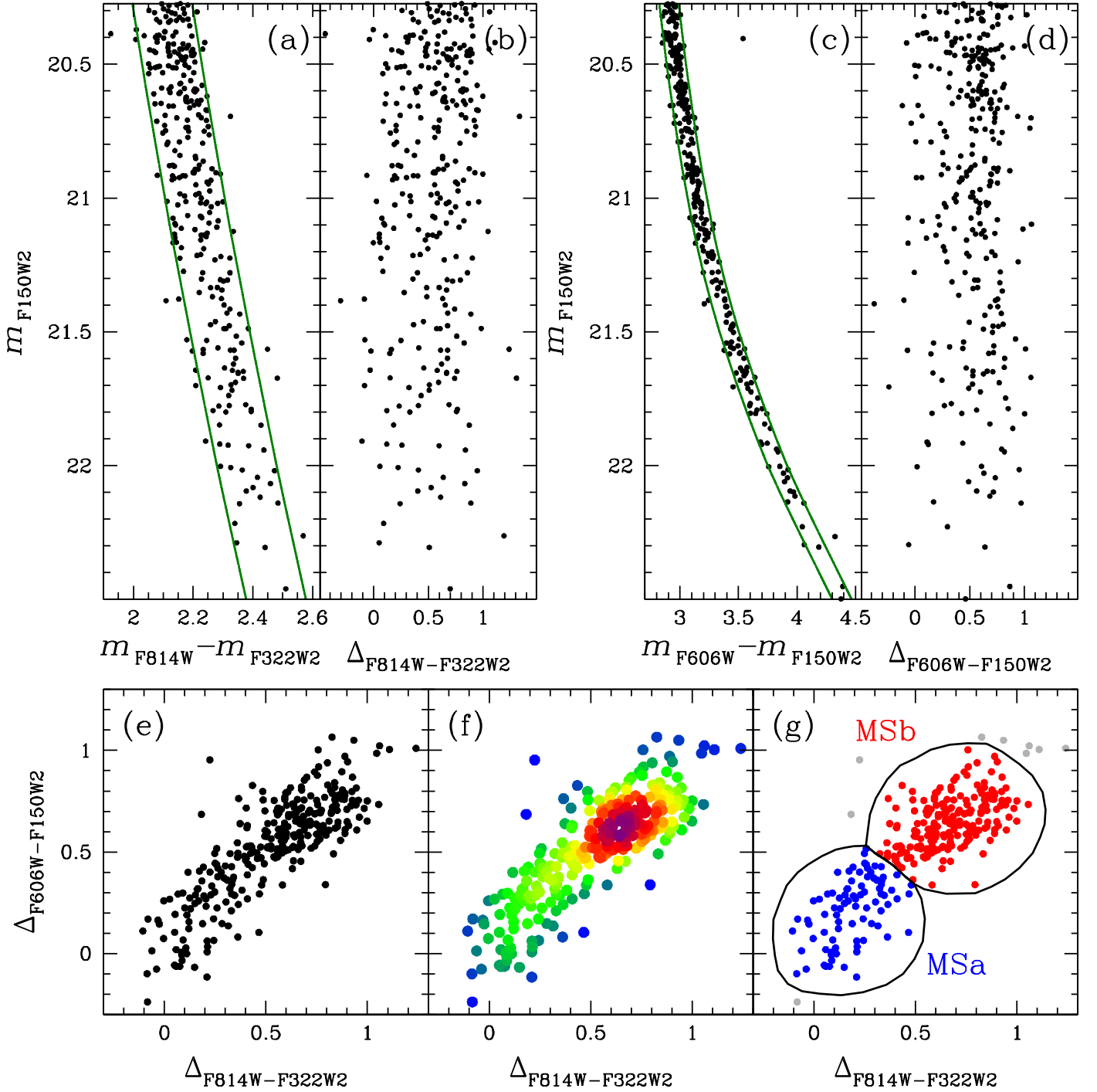
Fig. 2. Procedure used to identify the two sequences of stars in the lower part of the MS of NGC 6397. (a) m_{F150W2} versus $m_{\text{F814W}} - m_{\text{F322W2}}$ CMD of the stars in our sample, corrected for differential reddening and photometric zero-point variations. The two green lines (drawn by hand) are used to rectify the diagram. (b) Rectified m_{F150W2} versus $\Delta_{\text{F814W}-\text{F322W2}}$ CMD. (c)-(d) Same as (a)-(b) but for the m_{F150W2} versus $m_{\text{F606W}} - m_{\text{F150W2}}$ CMD. (e) $\Delta_{\text{F606W}-\text{F150W2}}$ versus $\Delta_{\text{F814W}-\text{F322W2}}$ TpCD. (f) Hess diagram of the TpCD. (g) The two stellar populations identified in the TpCD (within the black envelopes), MSa (in blue) and MSb (in red). Stars outside the black envelopes are represented in grey.

Panel (a) of Fig. 5 illustrates the spatial distribution of the two stellar populations in the X-Y plane. Points are colour-coded as in panel (g) of Fig. 2. The two populations show no clear difference in their spatial distributions.

We examined the radial profile of the relative number of the two populations by dividing the stars into two equally-populated radial bins. We then evaluated for each bin the ratio of the MSa population relative to the total number of stars in that bin. Panel (b) of Fig. 5 shows our measurements (filled circles) to-

gether with the values reported by Milone et al. (2012a, triangles) and Milone et al. (2017, squares) for the central part of the cluster. It is important to note that each dataset corresponds to different mass ranges (see discussion below). The combined dataset spans a radial distance from the centre of the cluster out to ~7 arcmin, corresponding to ~2.4r_{h}. This comprehensive analysis demonstrates that the two populations of NGC 6397 have reached complete spatial mixing. NGC 6397 has a half-mass relaxation time of t_{rh} ~0.5 Gyr (Vasiliev & Baumgardt
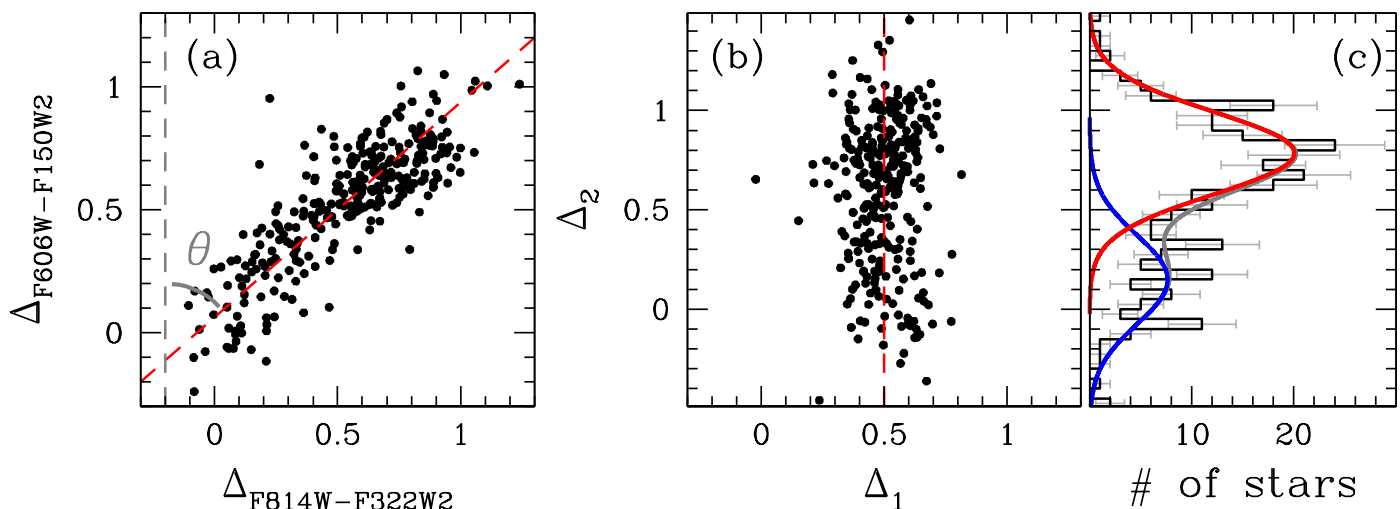
Fig. 3. (a) Same TpCD presented in panels (e) of Fig. 2. The red dashed line defines an angle θ with the y-axis. (b) Δ_2 versus Δ_1 diagram obtained by the counterclockwise rotation of panel (a) by an angle θ around the point (0.5,0.5). (c) Histogram of the Δ_2 distribution with error bars representing Poisson errors. The best-fitting double-Gaussian function is represented in grey, while the two components are plotted in blue and red.

2021) and is thus a dynamically old cluster (age/t_{rh} ~25; see also Giersz & Heggie 2009); various investigations studying the dynamical evolution of multiple-population clusters (see e.g. Vesperini et al. 2013, 2021; Dalessandro et al. 2019) predict that in clusters with this dynamical age the two populations should indeed be completely mixed and have lost memory of any initial spatial differences.

Finally, panel (c) presents the population ratio as a function of stellar mass. The average mass of the stars was inferred by means of the isochrones presented in Fig. 4. We divided our sample into two equally populated mass bins and evaluated the ratio of the MSa population in each bin. Our estimates are represented in panel (c) along with the values reported by Milone et al. (2012a) and Milone et al. (2017) using the same symbols as in panel (b). Similarly to what was found in the analysis of the radial distribution of the two populations, we find that the fraction of stars in the two populations is also independent of the stellar mass. This result is consistent, in general, with what was found for other clusters (e.g. Milone et al. 2019; Dondoglio et al. 2022; Milone et al. 2023; Ziliotto et al. 2023). Since in our analysis different mass intervals are studied in different radial regions we can not carry out a consistent analysis of the stellar mass function of the two populations and its radial variation (see e.g. King et al. 1995, for a study of mass segregation and radial variation of the stellar mass function in this cluster).

4. Conclusions

This paper represents the third instalment in a series, with a focus on the characterization of the mPOPs in NIR within the lower MS of NGC 6397 using high-precision photometry with *HST* and *JWST*. The TpCD highlights the presence of two components, namely MSa and MSb, associated with a primordial and second-generation population, respectively.

MSa and MSb are present in a ≈30-70 ratio, consistent with findings from previous studies of this GC focused on its centermost region. Combining the results in this work with those from the literature, we have found that the MSa/MSb ratio does not vary with the distance from the centre of the cluster; NGC 6397 is a dynamically old cluster and this finding is consistent with the results of numerical studies predicting that initial differences between the spatial distributions of mPOPs are gradually erased

during the cluster long-term evolution and expected to be completely lost in the dynamically older clusters.

The *JWST* near-infrared photometry data analysed in this paper, allowed us to probe and identify mPOPs in a low-mass interval (~ $0.09 - 0.18$ M$_\odot$) never studied before for this cluster. A comparison of our data with those of studies covering stellar mass intervals shows that the mass fraction is also independent of the stellar mass. This is consistent with what was found for other clusters (e.g. Milone et al. 2019; Dondoglio et al. 2022; Milone et al. 2023; Ziliotto et al. 2023) and could be used to put additional constraints on mPOP formation scenarios (see discussion in, e.g., Milone et al. 2023). Note that each of the three radial intervals analyzed for this cluster covers different mass intervals; the population ratio for different mass intervals is thus calculated at different radial distances; while we cannot a priori exclude the possibility that there are radial and mass dependencies cancelling each other and resulting in a population ratio independent of mass and radius, this would be an unlikely coincidence. For a comprehensive investigation of the stellar mass function and its radial variation, future observations providing data covering the same mass range at different radial distances will be necessary.

References

Baumgardt, H. & Vasiliev, E. 2021, MNRAS, 505, 5957
Bedin, L. R., King, I. R., Anderson, J., et al. 2008, ApJ, 678, 1279
Bedin, L. R., Piotto, G., Anderson, J., et al. 2004, ApJ, 605, L125
Bellini, A., Anderson, J., Bedin, L. R., et al. 2017a, ApJ, 842, 6
Bellini, A., Anderson, J., van der Marel, R. P., et al. 2017b, ApJ, 842, 7
Bellini, A., Libralato, M., Bedin, L. R., et al. 2018, ApJ, 853, 86
Brent, R. P. 1973, SIAM Journal on Numerical Analysis, 10, 327
Cadelano, M., Pallanca, C., Dalessandro, E., et al. 2023, A&A, 679, L13
Correnti, M., Gennaro, M., Kalirai, J. S., Cohen, R. E., & Brown, T. M. 2018, ApJ, 864, 147
Dalessandro, E., Cadelano, M., Vesperini, E., et al. 2019, ApJ, 884, L24
Dondoglio, E., Milone, A. P., Renzini, A., et al. 2022, ApJ, 927, 207
Gaia Collaboration, Prusti, T., de Bruijne, J. H. J., et al. 2016, A&A, 595, A1
Gaia Collaboration, Vallenari, A., Brown, A. G. A., et al. 2023, A&A, 674, A1
Gerasimov, R., Burgasser, A. J., Caiazzo, I., et al. 2024, ApJ, 961, 139
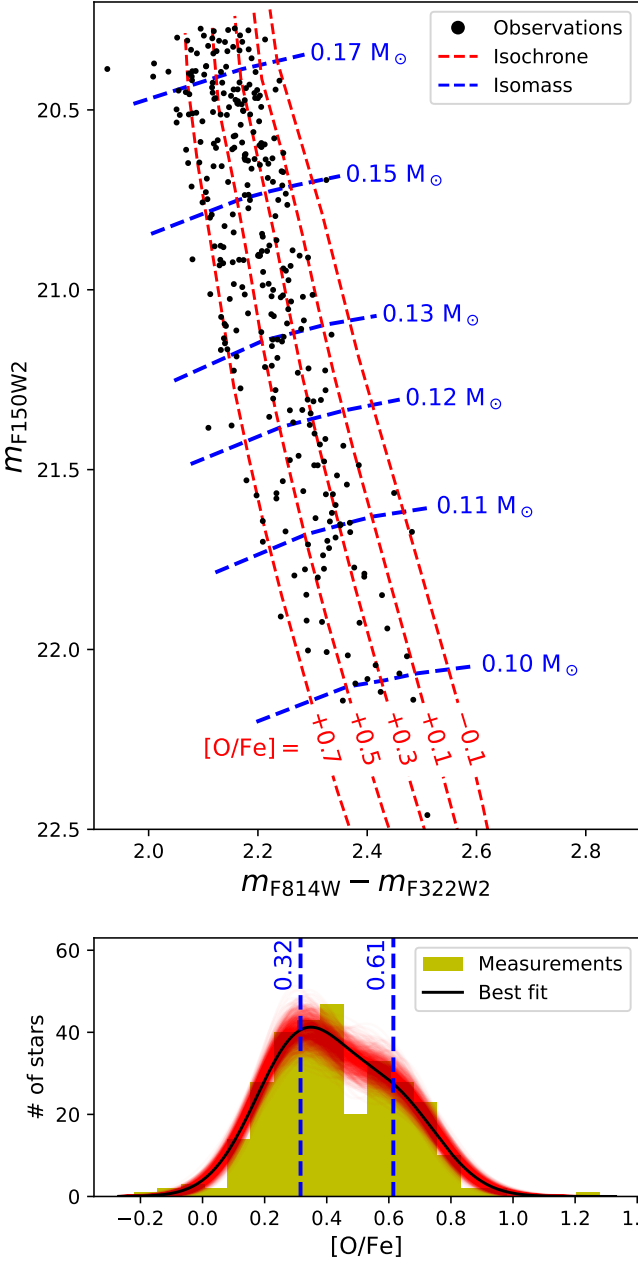
Libralato, M., Argyriou, I., Dicken, D., et al. 2024, PASP, 136, 034502
Libralato, M., Bellini, A., Bedin, L. R., et al. 2018, ApJ, 854, 45
Libralato, M., Bellini, A., van der Marel, R. P., et al. 2023, ApJ, 950, 101
Libralato, M., Bellini, A., Vesperini, E., et al. 2022, ApJ, 934, 150
Milone, A. P., Marino, A. F., Bedin, L. R., et al. 2019, MNRAS, 484, 4046
Milone, A. P., Marino, A. F., Dotter, A., et al. 2023, MNRAS, 522, 2429
Milone, A. P., Marino, A. F., Piotto, G., et al. 2012a, ApJ, 745, 27
Milone, A. P., Marino, A. F., Piotto, G., et al. 2015a, MNRAS, 447, 927
Milone, A. P., Marino, A. F., Piotto, G., et al. 2015b, ApJ, 808, 51
Milone, A. P., Piotto, G., Bedin, L. R., et al. 2012b, A&A, 540, A16
Milone, A. P., Piotto, G., Renzini, A., et al. 2017, MNRAS, 464, 3636
Nardiello, D., Bedin, L. R., Burgasser, A., et al. 2022, MNRAS, 517, 484
Nardiello, D., Bedin, L. R., Griggio, M., et al. 2023, MNRAS, 525, 2585
Nardiello, D., Libralato, M., Piotto, G., et al. 2018, MNRAS, 481, 3382
Pedregosa, F., Varoquaux, G., Gramfort, A., et al. 2011, Journal of Machine Learning Research, 12, 2825
Plez, B. 1998, A&A, 337, 495
Rieke, M. J., Kelly, D. M., Misselt, K., et al. 2023, PASP, 135, 028001
Sarajedini, A., Bedin, L. R., Chaboyer, B., et al. 2007, AJ, 133, 1658
Scalco, M., Bellini, A., Bedin, L. R., et al. 2021, MNRAS, 505, 3549
Scalco, M., Gerasimov, R., Bedin, L. R., et al. 2024, arXiv e-prints, arXiv:2403.03262
Vasiliev, E. & Baumgardt, H. 2021, MNRAS, 505, 5978
Vesperini, E., Hong, J., Giersz, M., & Hypki, A. 2021, MNRAS, 502, 4290
Vesperini, E., McMillan, S. L. W., D'Antona, F., & D'Ercole, A. 2013, MNRAS, 429, 1913
Ziliotto, T., Milone, A., Marino, A. F., et al. 2023, ApJ, 953, 62

Fig. 4. *Top:* model isochrones calculated in this study overplotted on NIRCam photometry of NGC 6397. The isochrones are labelled by the adopted oxygen abundance. Linearly interpolated isomass lines are shown for selected masses. *Bottom:* histogram of measured [O/Fe] values for the individual stars in the cluster. The best-fit two-component Gaussian mixture is overplotted, with the central values of both components indicated with vertical lines. The uncertainty in the best-fit distribution was estimated using 1000 bootstrap trials, shown with semi-transparent red lines.

Gerasimov, R., Burgasser, A. J., Homeier, D., et al. 2022, ApJ, 930, 24
Giersz, M. & Heggie, D. C. 2009, MNRAS, 395, 1173
Gratton, R., Bragaglia, A., Carretta, E., et al. 2019, A&A Rev., 27, 8
Gratton, R. G., Bragaglia, A., Carretta, E., et al. 2003, A&A, 408, 529
Griggio, M., Nardiello, D., & Bedin, L. R. 2023, Astronomische Nachrichten, 344, e20230019
Harris, W. E. 1996, AJ, 112, 1487
Harris, W. E. 2010, arXiv e-prints, arXiv:1012.3224
Husser, T.-O., Kamann, S., Dreizler, S., et al. 2016, A&A, 588, A148
Jørgensen, U. G., Jensen, P., Sørensen, G. O., & Aringer, B. 2001, A&A, 372, 249
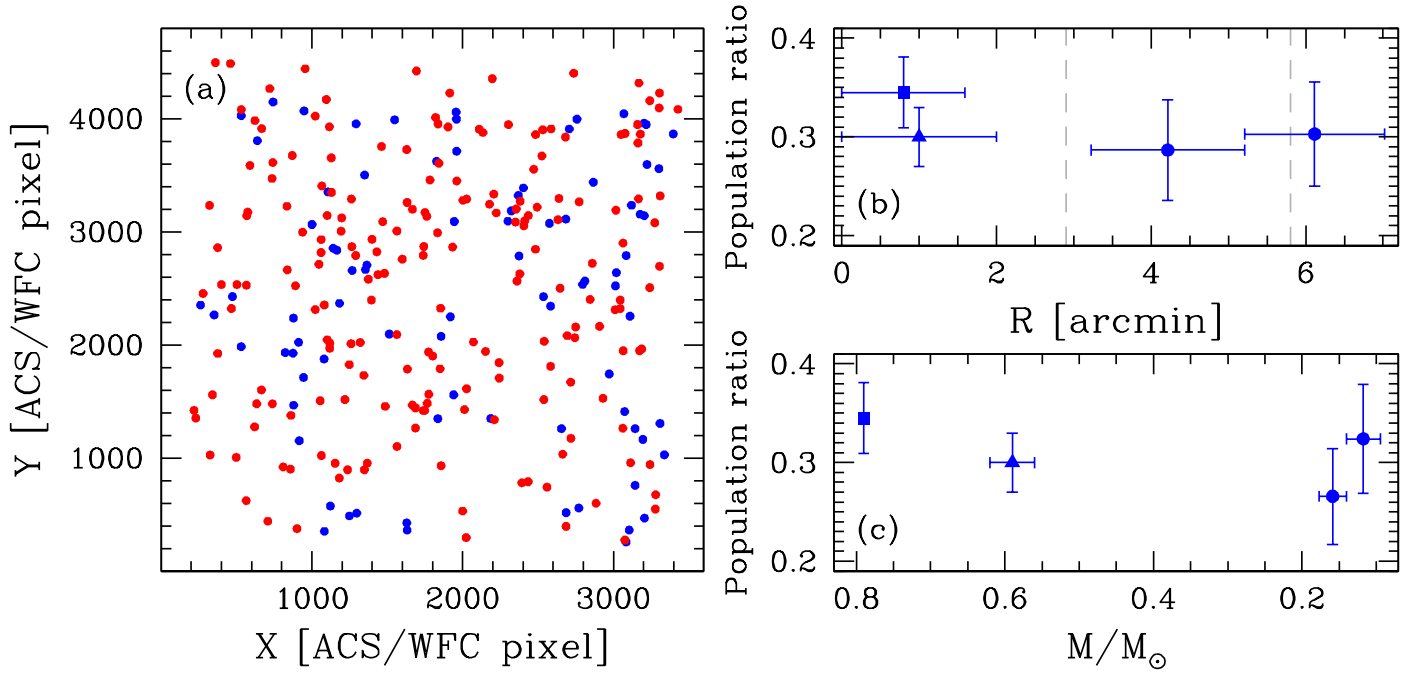King, I. R., Sosin, C., & Cool, A. M. 1995, ApJ, 452, L33

Fig. 5. (a) Spatial distribution of the two populations in the X-Y plane. Points are colour-coded as in panel (g) of Fig. 2. (b) Fraction of MSa stars as a function of radial distance from the centre of the cluster, R. The values obtained in this work are represented with circles, while the estimates from Milone et al. (2012a) and Milone et al. (2017) are shown with triangles and squares, respectively. Each dataset corresponds to different mass ranges (see panel (c)). The grey dashed lines are set at r_h and $2r_h$. (c) Fraction of MSa stars as a function of stellar mass. Symbols have the same meaning as in panel (b).